

**Nature of the ambient noise, site response and orientation of ocean bottom seismometers (OBSs): Scientific results of a passive seismic experiment in the Andaman Sea**

**Dewangan, P.<sup>1\*</sup>, Reddy, R.<sup>1</sup>, Kamesh Raju, K. A.<sup>1</sup>, Singha, P.<sup>1</sup>, Aswini, K. K.<sup>1</sup>, Yatheesh, V.<sup>1</sup>, Samudrala, K.<sup>1</sup>, Shuhail, M.<sup>1</sup>,**

<sup>1</sup> CSIR-National Institute of Oceanography, Dona Paula, Goa, 403004, India

**Abstract**

We analyze the nature of the ambient noise and site response for Ocean Bottom Seismometers (OBSs) deployed in the Andaman region. The probabilistic power spectral densities (PPSDs) of the OBSs show that the noise level in the Andaman region is within the range of Peterson's new low noise model (NLNM) and new high noise model (NHNM) for short periods (< 20 s). For long periods (> 20 s), the noise level is higher than NHNM. The peak associated with secondary microseisms occurs between 3 and 6 s. The stations that are close to the Andaman and Nicobar Islands show a prominent secondary microseismic peak at 4 s while the stations farther away show a small hump at 1 s. The noise level varies seasonally and shows a strong correlation with the significant wave height (SWH) computed from WAVEWATCH III. The ambient noise is down to -140 dB for the band from 0.1 s to 1 s, which provides the best signal-to-noise level for local earthquakes. For very short periods (< 0.1 s), the ambient noise level increases to -120 dB probably due to the efficient propagation of seismic energy through the low attenuation oceanic crust. The horizontal-to-vertical spectral ratio (HVSR) of the ambient noise curves shows an amplification factor greater than four. Furthermore, the HVSR curves show a broad/flat peak beneath the seamounts and the accretionary prism and a sharp/clear peak in the basinal area. We also estimate the orientation of the OBSs using Rayleigh wave polarization analysis.

## Introduction

The lack of seismological data from the oceanic region has limited the detailed understanding of Earth's interior beneath important geomorphic features. The incomplete seismological data in the oceans has resulted in a significant gap in seismic tomography restricting it from imaging the deep crustal and mantle structures. Most of the permanent seismological observatories are on land and yield poor ray coverage for large volumes of the Earth and at mid-mantle depths. Furthermore, the low and moderate seismicity occurring at oceanic plate boundaries often goes unnoticed due to the lack of such observatories. Scientists are developing the capability of Ocean Bottom Seismometers (OBSs) (Cox *et al.*, 1984; Webb and Crawford, 1999) and freely floating hydrophones (Simons *et al.*, 2009; Hello *et al.*, 2011) to overcome inhomogeneous distribution of observatories. However, the technical difficulties associated with the deployment of free fall OBSs pose several challenges for processing and interpretation of OBS data.

The main difficulty with free fall OBS deployment is to control the placement of the sensor on the ocean floor. Furthermore, the precise location of the OBS is also not known and is usually inferred from the deployment and recovery sites. Also, the OBS data show substantial low-frequency noise in comparison to that recorded from continental, coastal or island stations. The seafloor is noisy due to its proximity to natural sources such as ocean waves, wind and ocean currents. The three dominant oceanic noises observed on OBS data are long period noise ( $> 30$  s), primary microseisms with a dominant period of 14 s and secondary microseisms with a dominant period of 7 s. Long period noise occurs due to small wave height, long wavelength and long-period (30-500 s) ocean waves known as infragravity waves (Webb, 1998,2007; Ardhuin *et al.*, 2015; Doran and Laske, 2016). The primary microseisms are generated in shallow water where the water depth is lower than the wavelength of wind-forced gravity waves (Bromirski *et al.*, 2005). The nonlinear interaction of ocean waves traveling in opposite directions results in secondary microseisms (Longuet-Higgins, 1950). Double frequency microseismic waves have higher amplitude as compared to single frequency microseismic waves (Ardhuin *et al.*, 2011). The understanding of seismic noise will help in quantifying it and eventually removing it from the OBS data. The characterization of seismic noise is also required for selecting potential sites for permanent ocean floor seismic observatories and for temporary deployments of ocean bottom seismometer arrays (Wenz, 1962; Webb and Cox, 1986; Cox and Jacobs, 1989; D'Spain *et al.*, 1991; Babcock *et al.*, 1994; Webb, 1998).

The site-specific characterization (i.e., resonant frequencies and amplification factor) for OBSs is required for understanding the local geological conditions. The site-specific characterization is

usually carried out by analyzing the ambient noise records. The ratio of Fourier amplitude spectra of the horizontal and vertical components (Nakamura, 1989) is used to estimate the resonant frequency and amplification factor. The strength of the method lies in its stability; however, its theoretical basis is often debated (Mucciarelli and Gallipoli, 2001). Nakamura (1989, 2000) claimed that the HVSR method is related to S-wave resonance and it provides an estimate of site amplification factor. On the other hand, several authors argue that the method is related to the ellipticity of the Rayleigh wave and its interpretation regarding site amplification factor might be too simplistic (Lachet and Bard, 1994; Bard, 1998). There were no clear guidelines for the identification of peaks; therefore, the SESAME (Site EffectS assessment using AMbient Excitations) project proposed precisely such guidelines and discussed the possibilities and limitations of the method (Bard *et al.*, 2005).

Another problem associated with a free fall OBS is that its orientation is unknown. The information of an OBS's orientation is critical in studies related to seismic anisotropy, receiver functions and body- and surface-wave polarization utilizing the waveform data. The orientation of OBSs can be estimated by analyzing air gun or explosives shots, if available (Anderson *et al.*, 1987; Duennebier *et al.*, 1987). In the absence of controlled shots, the polarization analysis of teleseismic body waves and Rayleigh waves can be used to determine the orientation. Since the signal-to-noise ratio of surface wave arrivals is higher as compared to body wave arrivals, the Rayleigh wave polarization method outperforms the body wave polarization method (Stachnik *et al.*, 2012).

A passive OBS experiment was carried out in the Andaman region, northern Indian Ocean, to understand the seismicity pattern and geodynamic setting of the Andaman region. In the present study, we analyze the ambient noise records in the OBS data using probability density functions (McNamara and Buland, 2004) to characterize the noise in the northern Indian Ocean. We also studied the temporal variations of the amplitude of primary and secondary microseisms and compared them against various oceanographic parameters in the Andaman region. We compared the noise in the OBSs with the nearby island and coastal stations and also compared it with another similar experiment in the western Indian Ocean (Stähler, 2016). We also evaluated the site-specific characterization of the OBSs using the HVSR method following SESAME guidelines (Bard *et al.*, 2005) and interpreted the results according to the local geological conditions. Subsequently, we estimated the orientation of the OBSs using the polarization analysis of Rayleigh waves generated from teleseismic earthquakes.

## **PASSIVE SEISMIC EXPERIMENT IN THE ANDAMAN REGION**

The Andaman Sea extends from Myanmar in the north to Sumatra in the South and Malay

Peninsula in the east to Andaman and Nicobar Islands in the west. The Andaman basin shows many prominent morphological features such as the Barren and Narcondam volcanic islands, the invisible bank, and the Alcock and Sewell seamount complexes. Subduction of the Indian–Australian plate beneath the Southeast Asian plate occurs all along the Sunda arc, extending from the eastern Himalayan syntaxis to Banda arc, with major variations in speed and direction, resulting in oblique convergence in the Andaman–Nicobar sector. The effects of oblique plate convergence include strike-slip faulting parallel to the trench axis, formation of a sliver plate, backarc extension and basin formation. Subduction of the Indian plate along the Andaman arc, the formation of the Andaman–Nicobar ridge and the initiation of the spreading in the Andaman Sea are some of the important tectonic events that shaped the Andaman backarc basin (Kamesh Raju *et al.*, 2004).

Geophysical studies in the Andaman Sea (Kamesh Raju, 2005) have revealed a three-phase plate tectonic evolution of the Andaman backarc basin. Subduction of the Indian–Australian plate beneath the Southeast Asian plate occurring all along the Andaman arc is a significant tectonic event in the Andaman Sea. Due to limited geophysical data in the Andaman Sea, this subduction zone remains poorly understood. To fill the knowledge gap, we carried out a passive seismic OBS experiment in the Andaman region (Fig. 1). The compilation of the existing earthquake data from USGS after the destructive 26th December 2004 main shock helped in designing the location of OBSs. Two clusters of earthquakes located around (8°N, 94°E) and (12°N, 94°E) are chosen for the deployment of the OBSs so that we can observe a sufficient number of events in the OBS record.

We deployed twelve OBSs (OBS01 to OBS12) in the Andaman region during the last week of December 2013. We recovered all the OBSs during the second week of May 2014. Unfortunately, sensors in stations OBS04, OBS08, and OBS10 got stuck after deployment and failed to record any data. We strategically located the OBSs over important geomorphic features (Table 1). OBS01 and OBS12 lied on the Indian plate close to the subduction zone, OBS03 and OBS11 lied in the forearc basin, OBS09 lied on the Alcock seamount and OBS05 was on Sewell seamount. OBS06 and OBS07 lied on the Andaman back-arc spreading center (ABSC), and OBS02 was located off Nicobar Island where swarms of earthquakes are reported (Kamesh Raju *et al.*, 2012). The experiment was carried out with the wide band OBSs hired from the “LOBSTER” (Longterm OBS for Tsunami and Earthquake Research) program of K. U. M. Umwelt, Kiel, GmBH, Germany. We used the Güralp CMG-40T seismometer with a corner period of 60 s for the passive OBS experiment. The gimballed system was programmed to activate two days after landing on the seafloor, and after that leveling was carried out every 14 days.

## NATURE OF AMBIENT NOISE IN THE ANDAMAN REGION

We used probabilistic power spectral densities (PPSDs) to estimate the frequency-dependent statistics of the ambient noise for each OBS. PPSDs were computed using the method proposed by McNamara and Buland (2004) and implemented in SEISAN (Havskov and Ottemöller, 2009). The seismic data were divided into one-hour segments and FFTs were computed for each segment in an interval of 0.002 to 50 Hz. The PSDs were obtained from the amplitude spectra of the FFTs after accounting for the instrument response. The PSDs are represented in decibels with respect to the acceleration of  $1 \text{ m/s}^2$  and have units of  $(\text{m/s}^2)^2 / \text{Hz}$ . The PSDs were computed every 30 min with a 50 % overlap. The histogram of the PSDs are calculated for each period, and a probability density function (PDF) is estimated from the histogram at the bin center. We compared the noise record of the OBSs with the Peterson new high-noise model (NHNM) and new low-noise model (NLNM) (Peterson, 1993).

Figure 2 shows representative PPSDs for the three components of OBS09. We used cmocean colormap for plotting the spectra in GMT software (Wessel and Smith, 1998; Thyng *et al.*, 2016). The ambient noise level is within the range of the NHNM and NLNM for short periods ( $< 20 \text{ s}$ ). The dominant portion of the ambient noise is attributed to leaky Rayleigh waves (Ying *et al.*, 2014) having velocities comparable to or slightly lower than the S-wave velocity and are observed on almost all OBSs. For long periods ( $> 20 \text{ s}$ ), the noise level is slightly higher than the NHNM which we attribute to self-noise generated by the LOBSTER instrument. The peak associated with secondary microseisms occurs between 3 and 6 s similar to that observed in NHNM and NLNM. The low-noise notch, which has the best signal-to-noise ratio for teleseismic earthquakes, occurs between 8 and 20 s and the noise level is around -130 dB. The ambient noise is down to -140 dB for the band from 0.1 s (10 Hz) to 1 s (1 Hz) which gives the best signal-to-noise ratio for local earthquakes. The ambient noise increases again for very short periods ( $< 0.1 \text{ s}$ ) in the Andaman region. The gray line in Figure 2 highlights the mode ambient noise level. The noise on the horizontal components shows features similar to the vertical component, but it is higher by 5 to 10 dB probably due to the addition of tilt noise induced by ocean bottom currents (Crawford and Webb, 2000). In the low-noise notch band, the noise in the horizontal components is around -120 dB.

Figure 3 shows the mode noise level for all the OBSs for the vertical component. For long periods, the noise level for all the OBSs is comparable except OBS12 which shows an increase in noise to -100 dB at 100 s. The increase in noise level is attributed to the failure of the gimballed system as recorded in the engineering log data. OBS07 shows an unusually low noise level down to -138 dB at 100 s. The amplitude of the secondary microseisms depends on the location of the OBSs.

The stations OBS01, OBS12, OBS03, and OBS11 show relatively higher secondary microseism noise as they are closer to the coastline. Also, OBS09 has higher noise as it is close to the mountain chain formed due to arc volcanism. The stations OBS02, OBS05, OBS06, and OBS07 show no prominent secondary microseism peak as they are away from the islands. Instead, they show a small peak at around 1 Hz which may occur due to the interaction of waves at the ocean surface (Longuet-Higgins, 1950). This phenomenon can also be observed when multiple reflections cause the microseism group energy to propagate slowly in thickly sedimented oceanic regions (Ying *et al.*, 2014). The OBSs closer to the coast are expected to have higher amplitudes as the secondary microseisms are generated mainly due to the interaction of primary waves with the waves reflected from the coastline (Webb, 1998; Arduin *et al.*, 2015). The noise in the periods corresponding to the local earthquakes (0.1 to 1 s) is significantly higher in OBS06 which is located in the Andaman backarc spreading center (ABSC) suggesting enhanced seismicity in the vicinity of the spreading center. Moreover, OBS01 and OBS02 show higher noise for the short periods (0.1 to 0.2 s) probably associated with the enhanced local seismicity. For very short periods, the ambient noise increases in the Andaman region. The noise in this band usually comes from ship traffic, whales and other large mammals, and microearthquakes. The spectral analysis shows that the noise is spread across all the frequencies. Therefore, we attribute the increase in noise to the efficient propagation of Po and So phases (Webb, 1998) through the low attenuation oceanic crust located on both sides of the Andaman and Nicobar Islands. The OBSs show no systematic pattern in this frequency band. The horizontal components also show a pattern similar to that of the vertical component. The noise spectrum reveals that the North-South components of OBS03, OBS06 and OBS07 as well as the East-West component of OBS12 are out of the ordinary, which may be attributed to self-noise generated by the instruments. The high noise level on the vertical and horizontal components on OBS11 is probably due to tilt noises.

We also computed representative PPSDs for an island station (PBA), a coastal station (KUM) and a continental station (PKBT) to understand the propagation of ambient noise from the ocean to the continent (Fig. 4). The noise level of the continental station is very small and almost follows the NLNM. The noise level of the coastal station is comparable to the continental station. The island station has an intermediate noise level but slightly high as compared to continental and coastal stations. The OBSs appear to be noisier than the land stations. For long periods, the noise level decreases from -120 dB in OBSs to -150 dB in the island station which further decreases to -170 dB in the coastal and continental stations. The noise in this band is due to long period, small amplitude ocean waves which are known as 'infragravity waves.' The waves are most energetic on the shelf

(Webb, 2007), and the amplitude of the noise decreases as it propagates from ocean to continent as observed in the PPSDs. The strength of the secondary microseismic peak at 7 s is comparable between the OBSs and island station; however, it is reduced by 20 dB in the coastal and continental stations. Spectra examined from OBSs and continental station suggest that the double frequency microseisms rarely propagate from the deep ocean to land (Bromirski *et al.*, 2013). Ying *et al.*, (2014) observed that a significant portion of microseismic energy is reflected back by the continental slope. The noise in the very short period band is lowest in the coastal station and increases by 20 dB in the OBSs and continental station. It is strongest in the island station probably associated with human-induced cultural noise. Figure 5 compares the noise in the Andaman region, northern Indian Ocean, with that observed from the RHUM-RUM network in the western Indian Ocean (Stähler, 2016). In general, the noise in the Andaman region is smaller by 10 to 20 dB for long periods. The enhanced microseismic noise in the western Indian Ocean may be primarily attributed to the large noise produced by the high winds in the “roaring 40s” and the “screaming 50s” in the southern Indian Ocean (Webb, 1998). However, the noise in the very short periods is higher by 20-60 dB in the Andaman region. We attribute the increase in noise to the efficient propagation of Po and So phases (Webb, 1998) through the low attenuation oceanic crust. Noise observed in 20-100 s periods has similar trends in both the networks and may be attributed to self-noise generated by the LOBSTER instrument.

The noise spectra of OBSs vary not only with the spatial location but also with the seasons (Fig. 6). We computed the monthly trends of ambient noises including microseismic noises (primary and secondary) of each OBS by averaging the PPSDs over the months of January, February, March, and April. The microseism band occurs between 1 and 10 s with a dominant period of 4 s. In general, the strength of the microseismic noise varies with seasons due to the changes in the oceanographic conditions. We computed the daily variations of seismic noises by averaging PPSDs over a period of 24 hr. Microseisms are generated by wave interactions and are dependent on significant ocean wave heights (Webb, 1998). We attempt to establish a correlation between the wave heights and amplitudes of primary (0.05 – 0.08 Hz) and secondary microseisms (0.1 – 0.16 Hz). Significant wave height (SWH) represents the characteristics of a surface wave in the ocean. We obtained the SWH from the third-generation spectral wave model WAVEWATCH III version 4.18 (Tolman, 1991) for the deployment period around the Andaman region. In the large southern part of Indian Ocean, the model grid resolution is 0.5° x 0.5° (20° E -112° E and 70° S-5° N) whereas, in the northern Indian Ocean, the resolution is 0.1° x 0.1° (65° E-90° E and 5° N – 25° N). The model is forced with the ERA-Interim (Dee *et al.*, 2011) surface wind fields at six-hour intervals with a spatial resolution of 0.5°.

The resolution in wave direction is at 10°, and the wave frequencies are on a logarithmic scale from 0.04 to 0.5 Hz. The results of the model are validated with the measured wave data along the central west coast of India (Amrutha *et al.*, 2017). The SWH shows a strong correlation with the amplitudes of secondary microseisms (Fig. 7) with a correlation coefficient of 0.6. Enhanced noise is observed for the secondary microseisms on Julian days 55, 70, 90 and 110 of 2014. The strong correlation suggests that the SWH primarily governs the generation of secondary microseisms in the study area. The SWH shows negligible correlation (correlation coefficient of 0.1) with the primary microseisms.

### **SITE SPECIFIC CHARACTERIZATION USING HORIZONTAL TO VERTICAL SPECTRAL RATIO (HVSR)**

The horizontal-to-vertical spectral ratio (HVSR) of the ambient noise is widely used to study the local site effects (i.e., resonant frequencies and amplification factor) which depend on the nature of the sediments beneath the station. The HVSR method is independent of the magnitude of an event, source-station distance or source depth and depends only on the local site effect (Nakamura, 1989; Yamazaki and Ansary 1997; Mucciarelli and Gallipoli, 2001). Furthermore, the method is very stable and gives repeatable results when applied to background ambient noise. However, the interpretation of the result is not straightforward (Bonney-Claud *et al.*, 2006) therefore, the European SESAME project came out with guidelines for the implementation of HVSR. In the present study, we followed the SESAME guidelines and used the J-SESAME software (SESAME 2004) to determine the parameters of local site effects from the ambient noise records. The mean H/V curve was calculated using 190 noise records at each OBS. The noise records were selected randomly to get an unbiased sampling of the ambient noise. The H/V ratio is calculated for both the North-South (NS) and East-West (EW) components as well as for the average of the horizontal components computed from the geometric mean. We adopted the SESAME criteria to test the reliability of amplitude peaks and resonance frequency. We selected a window length of 30 s and record length of 1 hr (maximum 120 windows) so that we can meet the following criteria for a reliable H/V curve:

- i)  $f_0 > 10/L_W$  [ $f_0$  - Fundamental frequency;  $L_W$  - window length (30 s)]
- ii)  $n_c(f_0) > 200$  [ $n_c(f_0) = L_W \cdot n_W \cdot f_0$ ;  $n_W$  - Number of windows]
- iii)  $\sigma_A(f) < 2$  for  $0.5f_0 < f < 2f_0$  if  $f_0 > 0.5\text{Hz}$  [ $\sigma_A$  - standard deviation of  $A_{H/V}$  peak]

The standard deviation of  $A_{H/V}$  peak was found to be smaller than two for the resonance peak observed in all OBSs. Therefore, all the OBSs met the reliability criteria for the H/V curve. Furthermore, the resonance frequencies appear to be stable for different noise records.

In order to identify the clear peaks in the H/V curves, the following criteria are adopted as per



the SESAME guidelines:

- i)  $\exists f \in [f_0/4, f_0] \mid A_{H/V}(f) < A_0/2$  ( $f$  - frequency between  $f_0/4$  and  $f_0$ )
- ii)  $\exists f^+ \in [f_0, 4f_0] \mid A_{H/V}(f^+) < A_0/2$  ( $f^+$  - frequency between  $f_0$  and  $4f_0$ )
- iii)  $A_0 > 2$  [ $A_0$  - H/V peak amplitude at frequency  $f_0$ ]
- iv)  $f_{\text{peak}}[A_{H/V}(f) \pm \sigma_A(f)] = f_0 \pm 5\%$
- v)  $\sigma_f < \varepsilon(f_0)$  ( $\sigma_f$  - standard deviation of H/V peak frequency)
- vi)  $\sigma_A(f_0) < \theta(f_0)$  ( $\varepsilon(f_0)$ ,  $\theta(f_0)$  - Threshold value for the stability condition)

Table 2 gives the information about the SESAME criteria for the H/V peaks for the OBSs. The horizontal components which fulfill the clear H/V peak criteria are considered reliable and are interpreted with respect to the background geology.

The HVSR curve for the OBSs (Fig. 8) shows that most of the stations have a maximum amplification factor greater than four suggesting a high impedance contrast, a sharp discontinuity and a large shear-velocity contrast beneath the OBSs. We considered a single horizontal component for the stations OBS03, OBS06, OBS07 and OBS12 for the H/V ratio since the other horizontal component is not reliable. The HVSR curve shows two or more reliable peaks for OBS02, OBS06, OBS07 and OBS11 probably suggesting the occurrence of two or more layers of sharp S-wave impedance. It shows a broad peak at low frequencies close to 1 Hz for OBS05 and OBS09 suggesting multiple layers of sharp S-wave impedance. It shows a sharp peak for OBS03 and OBS12 indicating a strong impedance contrast between the sediments and the basement. The H/V curve for OBS02 failed to fulfill multiple criteria for a clear H/V peak and may not be reliable. The H/V curve of OBS03 satisfies all the criteria, and its resonance frequency is 2.8 Hz with an amplification factor of 8.4. The H/V curve of OBS05 shows two or more peaks, but only the peak at 4.5 Hz is reliable with an amplification factor of 3.3. The H/V curve of OBS06 exhibits three prominent peaks corresponding to resonance frequencies 2.2, 3.7 and 7 Hz. The peak at 2.2 Hz fails in criteria (i) and (ii) and is not reliable. The other peaks at 3.7 and 7 Hz with amplification factors of 6.95 and 2.31 fulfill five out of six criteria and are reliable. The low amplification value of the upper layer corresponding to resonance frequency 7 Hz implies reduced impedance contrast. The H/V curve of OBS07 also shows multiple peaks; however, only the peak at 4.5 Hz fulfills all the criteria with an amplification factor of 12.7. A high amplification factor suggests a large impedance contrast and a sharp discontinuity. The H/V curve of OBS09 shows a broad high with multiple peaks; however, none of the peaks are clear peaks as per the SESAME criteria. Similarly, the curve for

OBS11 shows multiple peaks and hence fails the criteria for a clear peak. The H/V curve of OBS12 has one clear peak at 7.2 Hz, and the corresponding amplification factor is 6.5.

We broadly classified the H/V curves into two categories – (i) curves showing broad/flat peaks at low frequencies which failed to meet the SESAME criteria (OBS05, OBS09, and OBS11), and (ii) curves showing sharp/clear peaks which meet the SESAME criteria (OBS03, OBS06, OBS07, and OBS12). It is interesting to note that the OBSs over the Alcock and Sewell seamounts (OBS09 and OBS05) and near the accretionary prism (OBS11) show a broad peak. In contrast, the OBSs near the subduction zone (OBS12), forearc basin (OBS03), and Andaman Backarc spreading center (OBS06 and OBS07) with thick sediment cover show a sharp and clear peak. Similar observations are reported offshore Mumbai where sites located on thick alluvium soil show a clear peak and those on basaltic rock show a broad peak (Surve and Mohan, 2010). The relative variation in resonance frequency is usually related to the sediment thickness (Seht and Wohlenberg, 1999). Within the sedimentary basin, the lowest frequency (2.8 Hz) is observed for OBS03 over the forearc basin indicating thick sedimentary cover. The sites over the ABSC show higher resonance frequencies of 3.7 and 4.5 Hz indicating shallower sedimentary cover. The largest resonance frequency (7.2 Hz) is observed for OBS12 suggesting a large S-wave impedance contrast at shallow depth. The significant amplification factor ( $> 5$ ) implies a sharp discontinuity with a large impedance contrast between the overlying and underlying sedimentary rocks.

## **ORIENTATIONS OF THE OBSs FROM THE RAYLEIGH WAVE POLARIZATION**

The user cannot control the deployment of a free fall OBS. Hence its orientation on the seafloor is unknown. We require the knowledge of the orientation of an OBS for advanced techniques like teleseismic receiver function, surface wave polarization, and shear wave splitting analysis. The orientation of the OBS can be estimated by both active (air gun) and passive sources (ambient noise and earthquakes). In the absence of active sources, the orientation of the OBS can usually be obtained by analyzing the P-wave or the Rayleigh wave recorded from teleseismic or local earthquakes. Several studies have highlighted the application of passive sources in estimating the orientation of OBSs. Stachnik *et al.* (2012) used the P-wave and Rayleigh wave from teleseismic events, Zha *et al.*, (2013) used the ambient noise, and Ekström and Busby (2008) used synthetic seismograms to estimate sensor orientations. In the present study, we used the polarization of teleseismic Rayleigh waves for determining the orientation of OBSs as proposed by Stachnik *et al.*, (2012). Due to the superior signal-to-noise ratio of the surface waves on the horizontal components, Rayleigh wave polarization analysis yields better results as compared to that of P-waves (Stachnik *et al.*, 2012).

Rayleigh waves are elliptically polarized in the vertical-radial plane, and the vertical motion is phase-shifted by  $90^\circ$  with respect to the radial component. The Hilbert transform of the vertical component yields a  $90^\circ$  phase shift so that a linear relationship can be achieved between the radial and vertical components. The cross-correlation between the Hilbert transformed vertical component and the radial component reveals the polarization of Rayleigh wave. The radial component is computed from the horizontal components for a range of back-azimuth directions ( $\theta$ ) assuming that one of the horizontal components is oriented in the north direction. The direction which gives the maximum correlation between the Hilbert transformed vertical component and the radial component represents the source-receiver back-azimuth which can be used to find the actual orientation of the OBS. We attempted the Rayleigh-wave polarization analysis using 30 teleseismic earthquakes with moment magnitude greater than 5.5 occurring during the deployment period (01<sup>st</sup> Jan 2014 to 15<sup>th</sup> May 2014) for the OBS stations OBS02, OBS05, OBS09, and OBS11. We used teleseismic earthquakes with an epicentral distance greater than  $20^\circ$  and signal-to-noise ratio, defined as the ratio of RMS amplitude after the onset of Rayleigh wave to the RMS amplitude before the beginning of the teleseismic event, greater than 2. A wide range of back azimuths has been considered to avoid bias in estimating the sensor orientations (Laske, 1995). We pre-processed the data by removing the mean, linear trend and the instrument response. We also applied a two pole and two pass Butterworth filter with corner frequencies of 0.03 - 0.1 Hz for enhancing the Rayleigh wave.

One of the essential requirements of the method is the windowing of the Rayleigh wave phase. We adopted two approaches for estimating Rayleigh window: a) we manually picked the Rayleigh window where the amplitude of the vertical component was comparable to the radial component, and b) we predicted the arrival window of the Rayleigh wave assuming a group velocity of 2.7 to 3.8 km/s. After selecting the Rayleigh window, we rotated the E-W and N-S components into radial-transverse coordinates using the equation:  $\begin{pmatrix} R \\ T \end{pmatrix} = \begin{pmatrix} \cos \theta & \sin \theta \\ -\sin \theta & \cos \theta \end{pmatrix} \begin{pmatrix} EW \\ NS \end{pmatrix}$ , where  $\theta$  represents the back-azimuth direction. The  $\theta$  which maximizes the cross-correlation coefficient between the Hilbert-transform vertical component and the radial component ( $C_{zr}^* = \frac{S_{zr}}{S_{zz}}$ ) represents the estimated back-azimuth direction. We also used normalized cross correlation  $C_{zr} = \frac{S_{zr}}{\sqrt{S_{zz}S_{rr}}}$  for quality control. The sensor orientation (X) can be obtained by subtracting the back-azimuth from the source-to-event azimuth (seaz) i.e.,  $X = \text{seaz} - \theta$ . Figure 9 shows the graphical illustration of the methodology. The relationship between the back-azimuth and source-to-receiver azimuth is shown in

Figure 9a. Representative normalized and unnormalized cross-correlation coefficients between the Hilbert-transform vertical component and the radial component are shown in Figure 9b. The quality control (QC) plot shows the Hilbert-transform vertical and the radial components (Fig. 9c). A good match between the two components indicates that the estimated back-azimuth is close to the actual back-azimuth. Orientations of the stations OBS02, OBS05, OBS09, and OBS11 estimated from the Rayleigh wave polarization technique are represented using a polar plot (Fig. 10). The estimated orientations for the OBSs are consistent for different teleseismic earthquakes with various source-to-event azimuths. The orientation will be useful for advanced techniques like the teleseismic receiver function, surface wave polarization and shear wave splitting analysis.

## CONCLUSIONS

In the present study, we analyzed the nature of the ambient noise in the Andaman region from OBS data. The PPSDs of the ambient noise show that the noise level is within the NLNM and NNNM for short periods ( $< 20$  s). The PPSDs for very long periods ( $> 20$  s) show increased noise probably due to the noise generated by the instrument. We observed the peak associated with secondary microseisms at 4 s for the stations (OBS01, OBS12, OBS03, and OBS11) closer to the Andaman and Nicobar Islands suggesting that the noise is strongest along the coastlines. The stations away from the coast (OBS02, OBS05, OBS06, and OBS07) show a small peak at 1 s which is probably due to the interaction of ocean waves at the ocean surface. The strength of the noise varies temporally and shows a strong correlation with the SWH, indicating that wave height may govern the generation of secondary microseism noise along the coast. No such correlation is observed for the primary microseisms. The ambient noise is lowest between the periods 0.1 and 1 s which gives the best signal-to-noise ratio for local earthquakes. The noise increases again for very short periods ( $< 0.1$  s) which might be due to the efficient propagation of earthquake energy through the low attenuation oceanic crust. In general, the long period ambient noise decreases from the ocean to the island/coastal and continental stations. However, the microseismic noise is comparable between the OBSs and island stations but decreases by 20 dB for the coastal and continental stations. The noise in the Andaman region is smaller by 10 to 20 dB as compared to that observed in the western Indian Ocean.

We estimated the HVSF curves for the OBSs and interpreted them as per the SESAME guidelines. The stations lying on the hard rocks, i.e., on the Alcock and Sewell seamounts and near the accretionary prism show a broad peak. However, the stations within the sedimentary basin, i.e., near the subduction zone, forearc basin, and in the Andaman backarc spreading center show a sharp peak with resonance frequency varying from 2.8 Hz to 7.2 Hz. A large amplification factor ( $> 5$ )

suggests the presence of a sharp shear wave contrast between the overlying and underlying sedimentary rocks.

## DATA AND RESOURCES

We carried out a passive seismic experiment to understand the seismicity and geodynamic setting in the Andaman region. Twelve broadband ocean bottom seismometers (OBS) with a corner period of 60 s were deployed during the last week of December 2013 and recovered during the second week of May 2014. Unfortunately, three OBSs got stuck after deployment and did not record any data. The locations of the OBSs were selected based on the past seismicity map and geomorphology of the Andaman region covering the Andaman subduction zone, forearc basin, Alcock and Sewell seamounts, Andaman backarc spreading center (ABSC) and off Nicobar region where swarms of earthquakes are reported. The OBSs recorded numerous local and teleseismic earthquakes during the deployment period. They also recorded the aftershock sequence of a major earthquake (6.2 Mb: origin time 13:41 21<sup>st</sup> Mar 2014) off Nicobar from 21<sup>st</sup> – 23<sup>rd</sup> Mar 2014.

## ACKNOWLEDGEMENT

We thank the Director, CSIR-NIO for supporting the study. We are grateful to the crew on board *RV Sindhu Sankalp* and the ship cell of CSIR-NIO for their assistance during the deployment and recovery operations of the OBSs on the cruises. We would like to thank the Director, ESSO-INCOIS for providing the PBA data. Earthquake data for the KUM and PBKT station were compiled from the International Seismological Centre (ISC). The author Ramakrishna Reddy acknowledges the Science and Education Research Board (SERB) for the support towards a National Postdoctoral Fellowship (NPDF). We thank Dr. Sanil Kumar for providing the wave-height data in the Andaman region. We are grateful to Mr. Arne Schwenk, K.U.M. Umwelt- und Meerestechnik Kiel GmbH for his excellent work during the OBSs deployment and recovery operations. We thank the anonymous reviewers and the associate editor for their comments/suggestions which have improved the quality of the manuscript. The work was performed under the GENIAS project of CSIR-NIO. This is CSIR-NIO contribution no. xxx.

## REFERENCES

- Amrutha, M.M., V. Sanil Kumar, and Jesbin George (2017). Observations of long-period waves in the nearshore waters of central west coast of India during the fall inter-monsoon period, *Ocean Engineering*. **131**, 244-262.
- Anderson, P.N., F.K. Duennebieer, and R.K. Cessaro (1987). Ocean borehole horizontal seismic sensor orientation determined from explosive charges, *J. Geophys. Res. Solid Earth*. **92**, no. B5, 3573–3579.

- Ardhuin, F., E. Stutzmann, M. Schimmel, and A. Mangeney (2011). Revealing ocean wave sources of seismic noise, *Journal of Geophysical Research*. **116**, no. C9.
- Ardhuin, F., L. Gualtieri, and E. Stutzmann (2015). How ocean waves rock the Earth: Two mechanisms explain microseisms with periods 3 to 300s, *Geophys. Res. Lett.* **42**, no.3, 765–772.
- Babcock, J. M., B. A. Kirkendall, and J. A. Orcutt (1994). Relationships between ocean bottom noise and the environment, *Bull. Seismol. Soc. Am.* **84**, no.6, 1991–2007.
- Bard, P. Y., A. M. Duval, B. Lebrun, C. Lachet, J. Riepl, and D. Hatzfeld (1997). Reliability of the H/V technique for site effects measurement: An experimental assessment, Proceedings of 8th International Conference on Soil Dynamics and Earthquake Engineering, Istanbul, 20–24 July 1997.
- Bard, P.-Y., (1998). Microtremor measurement : a tool for site effect estimation? K. Irikura K. Kudo H. Okada T. Sasatami Eds **3**, 1251–1279.
- Bard, P. Y., and SESAME-Team (2005) Guidelines for the implementation of the H/V spectral ratio technique on ambient vibrations: measurements, processing, and interpretations. *SESAME European research project*.
- Bonnefoy-Claudet, S., F. Cotton, and P. Y. Bard (2006). The nature of noise wavefield and its applications for site effects studies. A literature review. *Earth-Science Rev.* **79**, no.3, 205–227.
- Bromirski, P. D., F. K. Duennebieer, and R. A. Stephen (2005). Mid-ocean microseisms, *Geochem. Geophys. Geosyst.* **6**.no.4.
- Bromirski, P. D., R. Stephen, and P. Gerstoft (2013). Are deep-ocean-generated surface-wave microseisms observed on land? *Journal of Geophysical Research: Solid Earth*. **118**, no.7, 3610–3629
- Cox, C. S., and D. C. Jacobs (1989). Cartesian diver observations of double frequency pressure-fluctuations in the upper levels of the ocean, *Geophys. Res. Lett.* **16**, no.8, 807 – 810.
- Cox, C., T. Deaton, and S. Webb (1984). A Deep-Sea Differential Pressure Gauge, *J. Atmos. Ocean. Technol.* **1**, no.3, 237-246
- Crawford, W. C., and S. C. Web (2000). Identifying and removing tilt noise from low-frequency (< 0.1 Hz) seafloor vertical seismic data. *Bull. Seismol. Soc. Am.* **90**, no.4, 952-963.
- D’Spain, G. L., W. S. Hodgkiss, and G. L. Edmonds (1991). The simultaneous measurement of infrasonic acoustic particle-velocity and acoustic pressure in the ocean by freely drifting Swallow floats, *IEEE J. Oceanic Eng.* **16**, no.2, 195 – 207.
- Doran, A.K., and G. Laske (2016). Infragravity waves and horizontal seafloor compliance, *J. Geophys. Res. Solid Earth*. **121**, no.1, 260–278.
- Dee, D. P., S.M. Uppala, A.J. Simmons, P. Berrisford, P. Poli, S. Kobayashi and P. Bechtold (2011). The ERA-Interim reanalysis: Configuration and performance of the data assimilation system, *Q. J. R. Meteorolog. Soc.* **137**, no. 656, 553-597.
- Duennebieer, F.K., P.N. Anderson, and G.J. Fryer (1987). Azimuth determination of and from horizontal ocean bottom seismic sensors, *J. Geophys. Res.* **92**, no.B5, 3567-3572.

- Ekström, G., and R. W. Busby (2008). Measurements of seismometer orientation at USArray Transportable Array and Backbone stations, *Seismol. Res. Lett.* **79**, no.4, 554–561
- Havskov, J., and L.Ottmøller (2009). Introduction to SEISAN and Computer exercises in processing earthquake data.
- Hello, Y., A.Ogé, A. Sukhovich, and G. Nolet (2011). Modern mermaids: New floats image the deep Earth. *Eos, Transactions American Geophysical Union*, **92**, no.40, 337–338.
- Kamesh Raju, K. A., T. Ramprasad, P. S. Rao, B. R. Rao, and J. Varghese (2004). New insights into the tectonic evolution of the Andaman basin, northeast Indian Ocean, *Earth Planet Sci. Lett.* **221**, no.1, 145–162.
- Kamesh Raju, K.A. (2005). Three-phase tectonic evolution of the Andaman backarc basin, *Curr. Sci.* **89**, no.11, 1932–1937.
- Kamesh Raju, K.A., D.Ray, A.Mudholkar, G.P.S.Murty, V.K.Gahalaut, K. Samudrala, A.L. Paropkari, R.Ramachandran, and L.Surya Prakash (2012). Tectonic and volcanic implications of a cratered seamount off Nicobar Island, Andaman Sea, *J. Asian Earth Sci.* **56**, 42–53.
- Lachet, C., and P.-Y. Bard (1994). Numerical and Theoretical Investigations on the Possibilities and Limitations of Nakamura's Technique, *J. Phys. Earth.* **42**, no.5, 377–397.
- Laske, G., (1995). Global observation of off-great-circle propagation of long-period surface waves, *Geophys. J. Int.* **123**, no.1, 245–259
- Longuet-Higgins, M. S., (1950). A theory of the origin of microseisms, *Phil. Trans. Roy. Soc.* **243**, no.857, 1–35.
- McNamara, D. E., and R. Buland (2004). Ambient Noise Levels in the Continental United States, *Bull. Seismol. Soc. Am.* **94**, no.4, 1517– 1527.
- Mucciarelli, M., and M.R.Gallipoli (2001). A critical review of 10 years of Nakamura technique, *Boll. Geof. Teor. Appl.* **42**, no. 3-4, 255–266.
- Nakamura, Y., (2000). Clear identification of fundamental idea of Nakamura's technique and its applications.1-8
- Nakamura, Y., (1989). A method for dynamic characteristics estimation of subsurface using microtremor on the ground surface, *Q. Rep. Railw. Tech. Research Inst.* **30**, no.1, 25–33.
- Peterson, J., (1993). Observation and modelling of seismic background noise, *U.S. Geol. Surv. Tech. Rept.* 93–95.
- Seht, M.I.V., and J.Wohlenberg (1999). Microtremor Measurements Used to Map Thickness of Soft Sediments, *Bull. Seismol. Soc. Am.* **89**, no.1, 250–259.
- Simons, F.J., G.Nolet, P.Georgief, J.M.Babcock, L.a.Regier, and R.E. Davis (2009). On the potential of recording earthquakes for global seismic tomography by low-cost autonomous instruments in the oceans, *J. Geophys. Res.* **114**, no.B5, 1–16.

- Stachnik, J. C., A. F. Sheehan, D. W. Zietlow, Z. Yang, J. Collins, and A. Ferris (2012). Determination of New Zealand ocean bottom seismometer orientation via Rayleigh-wave polarization, *Seismol. Res. Lett.*, **83**, no.4, 704–713.
- Stähler, S.C., (2016). Performance report of the RHUM-RUM ocean bottom seismometer network around La Réunion , western Indian Ocean Performance report of the RHUM-RUM ocean bottom seismometer network around La Réunion , western Indian Ocean, *Advances in geosciences*.**41**, 43-63.
- Surve G., and G.Mohan (2010). Site response studies in Mumbai using (H/V) Nakamura technique, *Nat Hazards*.**54**, no.3, 783–795.
- Thyng, K.M., C.A. Greene, R.D. Hetland, H.M. Zimmerle, and S.F. DiMarco (2016). True colors of oceanography: Guidelines for effective and accurate colormap selection, *Oceanography*. **29**, no.3, 9–13.
- Tolman, H. L.,(1991). A third-generation model for wind waves on slowly varying, unsteady and inhomogeneous depths and currents, *J. Phys. Oceanogr.* **21**, no.6, 782–797.
- Webb, S. C., (1988). Long-period acoustic and seismic measurements and ocean floor currents, *IEEE J. Oceanic Eng.* **13**, no.4, 263 – 270.
- Webb, S. C., (1998). Broadband seismology and noise under the ocean, *Rev.Geophys.* **36**, no.1, 105 – 142.
- Webb, S. C., and C. S. Cox (1986). Observations and modeling of seafloor microseisms, *J. Geophys. Res.* **91**, no.B7, 7343 – 7358
- Webb, S.C., (2007). The Earth’s “hum” is driven by ocean waves over the continental shelves, *Nature*. **445**, no.7129, 754–756.
- Webb, S.C., and W.C.Crawford (1999). Long-period seafloor seismology and deformation under ocean waves, *Bull. Seismol. Soc. Am.* **89**, no.6, 1535–1542.
- Wenz, G. M., (1962). Acoustic ambient noise in the ocean: Spectra and sources, *J. Acoust. Soc. Am.* **34**,no.12, 1936-1956.
- Wessel, P., and W.H, Smith (1998). New, improved version of Generic Mapping Tools released. *Eos, Transactions American Geophysical Union*. **79**, no.47, 579-579.
- Yamazaki, F., and M. A. Ansary (1997). Horizontal-to-vertical spectrum ratio of earthquake ground motion for site characterization, *Earthq. Eng. Struc. Dyn.* **26**, no.7, 671–689.
- Ying, Y., C. J. Bean, and P. D. Bromirski (2014). Propagation of microseisms from the deep ocean to land, *Geophys. Res. Lett.* **41**, no.18, 6374–6379.
- Zha, Y., S. C. Webb, and W. Menke (2013). Determining the orientations of ocean bottom seismometers using ambient noise correlation, *Geophys. Res. Lett.* **40**,no.14,355-3590.



### **Full mailing address for each other**

Pawan Dewangan (Senior Scientist)  
National Institute of Oceanography (NIO), Goa  
Email:pdewangan@nio.org

Ramakrushana Reddy. T (Postdoctoral Fellow)  
NIO, Goa.  
Email:ramareddy@nio.org

Kamesh Raju K.A (chief Scientist)  
NIO ,Goa.  
Email: kamesh@nio.org

Pabitra Singha (Ph.D Scholar)  
NIO , Goa.  
Email:psingha@nio.org

Aswini. K (Ph.D Scholar)  
NIO, Goa.  
Email: aswinik@nio.org

Yatheesh. V (Scientist)  
NIO, Goa.  
Email:yatheesh@nio.org

Samudrala. K (Technical Assistant)  
NIO,Goa.  
Email: samudrala@nio.org

Shuhail. M (PhD Scholar)  
NIO,Goa.

Email: mshuhail@nio.org

### **List of figure captions**

1. Location map of study area. OBS stations are represented with stars and land stations are marked with inverted triangles. Zoom out of the study area is shown in the inset.
2. Comparison of noise levels on three components of OBS09 station in the month of April.
3. Vertical spectral mode noise of all nine OBS stations.
4. Comparison of noise level of OBS stations with the referenced land stations. The lower and upper black curves are the low and high noise models of Peterson (1993).
5. Comparison of Andaman network with RHUM-RUM Network. Right part of the figure is reproduced from the noise spectral plots of Rhum-Rum network and left part of the figure is from Andaman network (OBS09).
6. Monthly trends of the seismic noise at the station OBS09 in Andaman for the three components (Z, N, E), indicated in the upper left corner of each plot.
7. Correlation of primary and secondary microseisms with the significant wave heights at OBS 03.
8. Site response parameters (fundamental frequency and amplification factor) of OBS stations using HVSR. Solid line is the mean curve (H/V) and dashed lines are  $H/V \cdot sd$  and  $H/V/sd$  (sd: standard deviation).
9. Working methodology of estimation of horizontal orientations of OBS stations. (a) Coordinate system and terms used to determine the accurate horizontal orientation of OBS stations. (b) Correlation coefficient between  $C_{rz}$  and  $C_{zz}$  as a function of possible orientation angle. Correlation coefficient is used to determine the orientation angle; Normalized correlation coefficient  $C_{rz}$  is for quality control; vertical line represents maximum  $C_{rz}$  at which the orientation is measured. (c) Correlation between radial and Hilbert transformed vertical for a given orientation obtained in (b)
10. Polar orientation of four OBS stations measured from 30 teleseismic events; Arrow represents the mean orientation.

### **List of table captions**

Table. 1. Location, depth and geological settings of OBS stations in the Andaman region.

Table. 2. SESAME criteria for the identification of clear and reliable H/V peaks for the OBS stations.

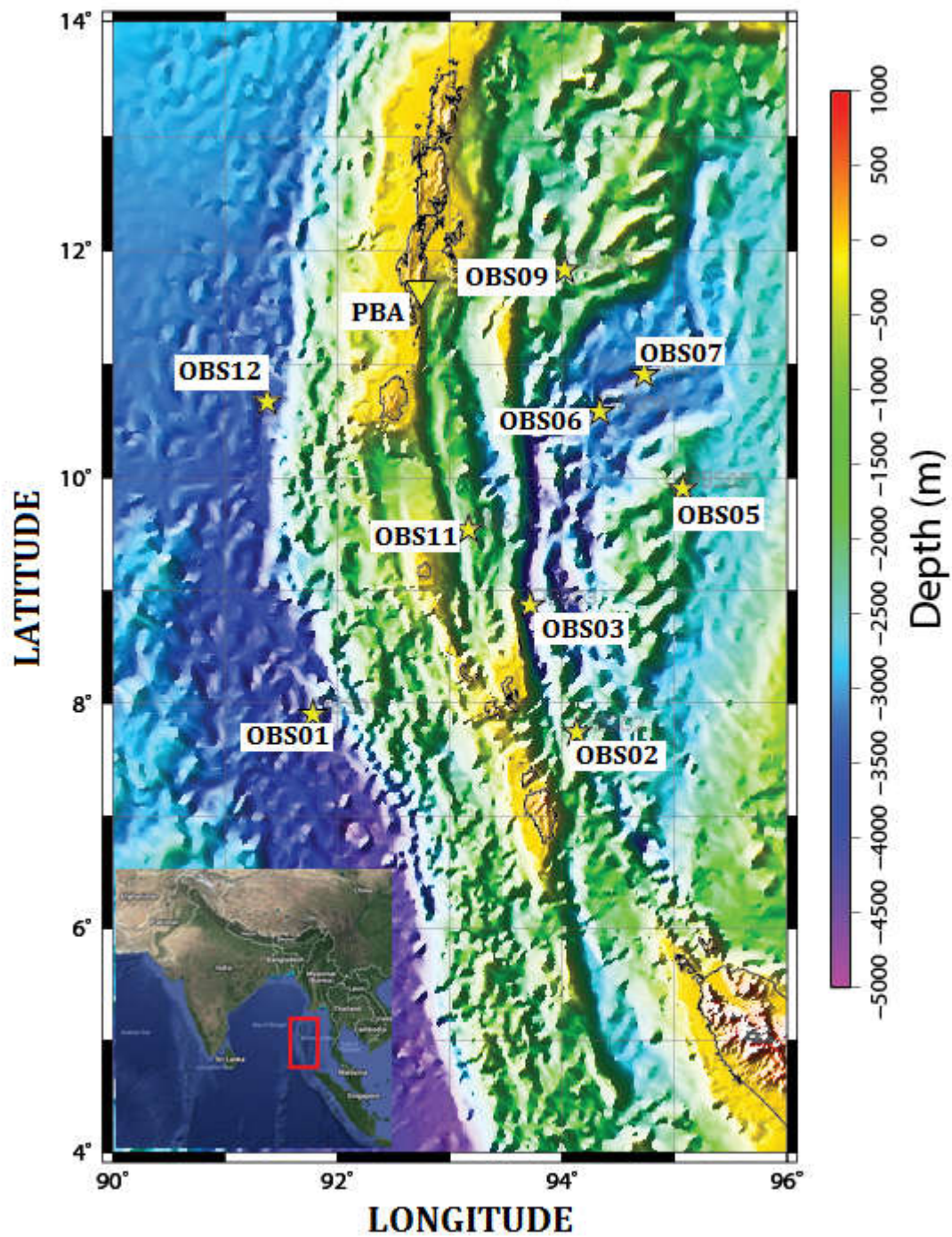


Figure 1. Location map of study area. OBS stations are represented with stars and land stations are marked with inverted triangles. Zoom out of the study area is shown in the inset.

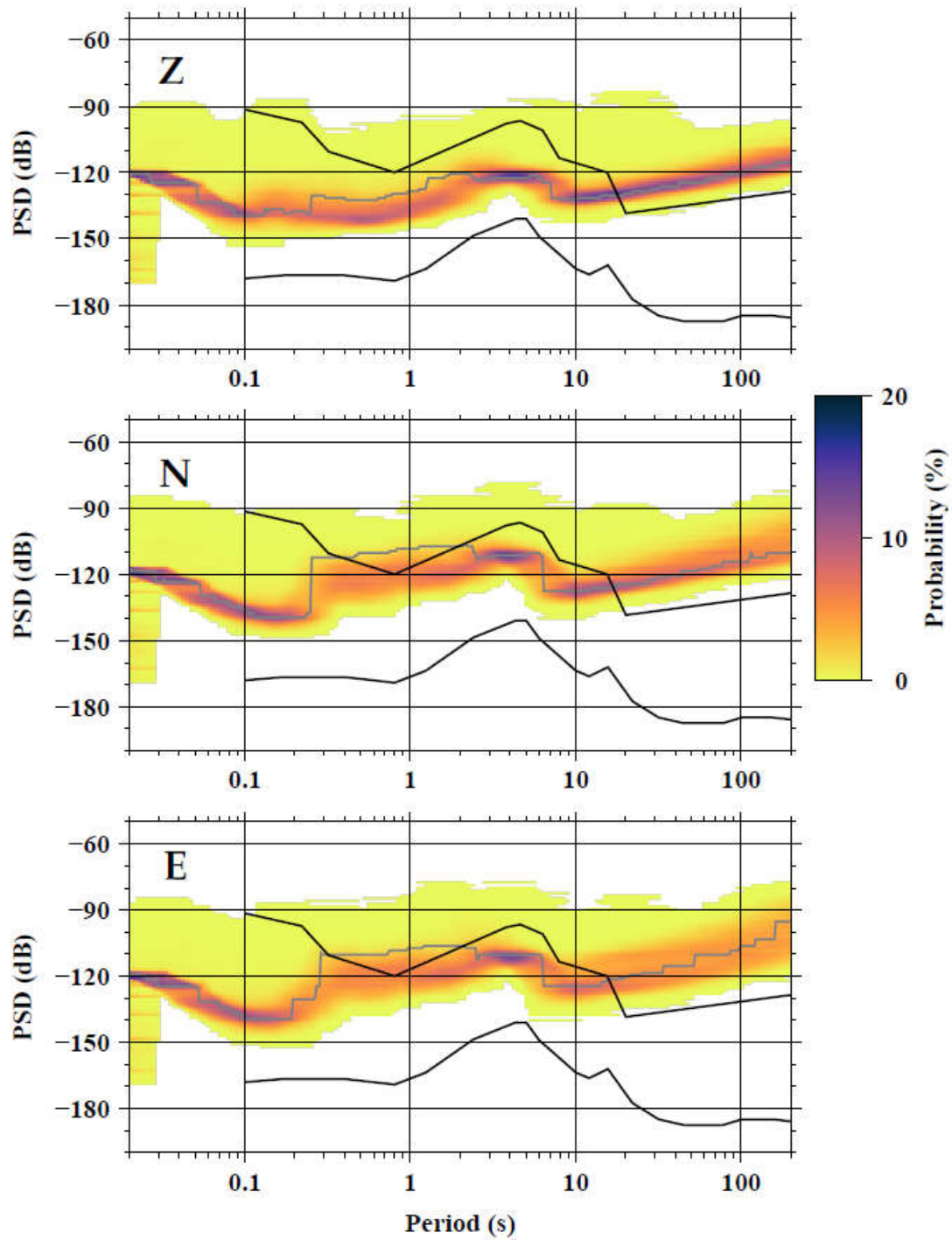


Figure 2. Comparison of noise levels on three components of OBS09 station in the month of April.

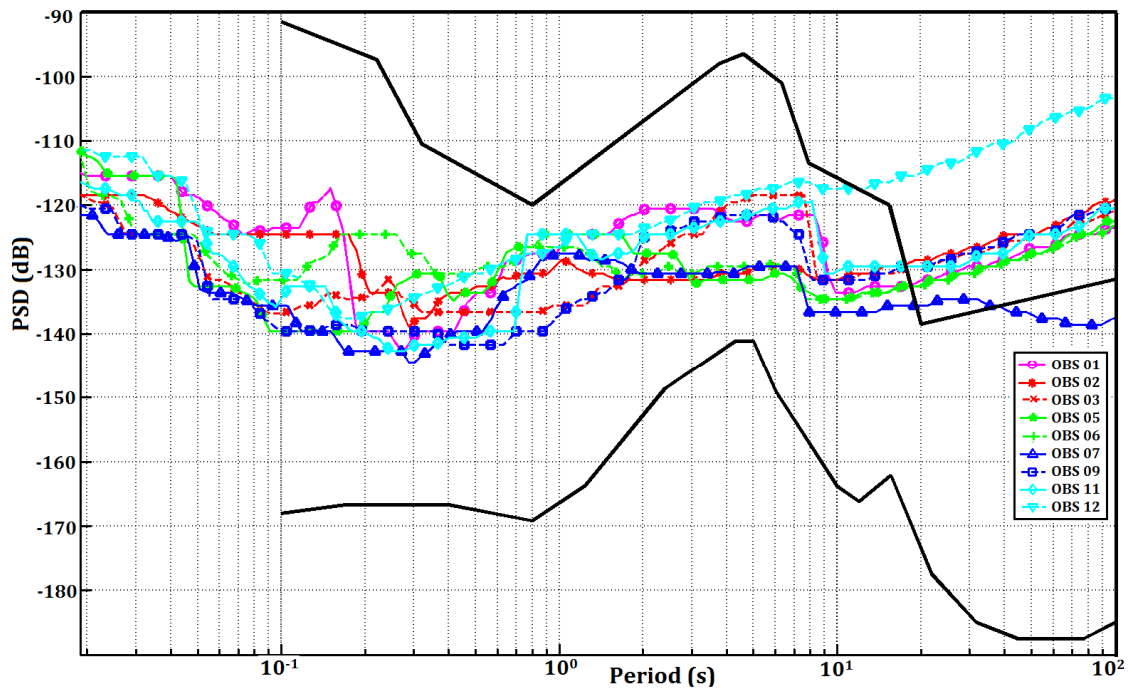


Figure 3. Vertical spectral mode noise of all nine OBS stations.

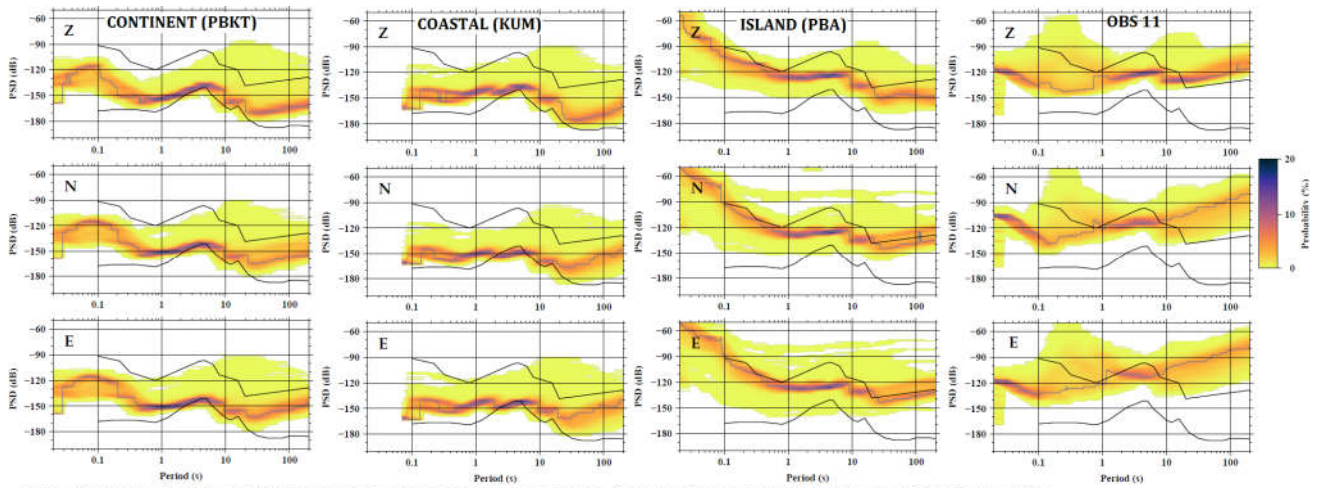


Figure 4. Comparison of noise level of OBS stations with the referenced land stations. The lower and upper black curves are the low and high noise models of Peterson (1993).



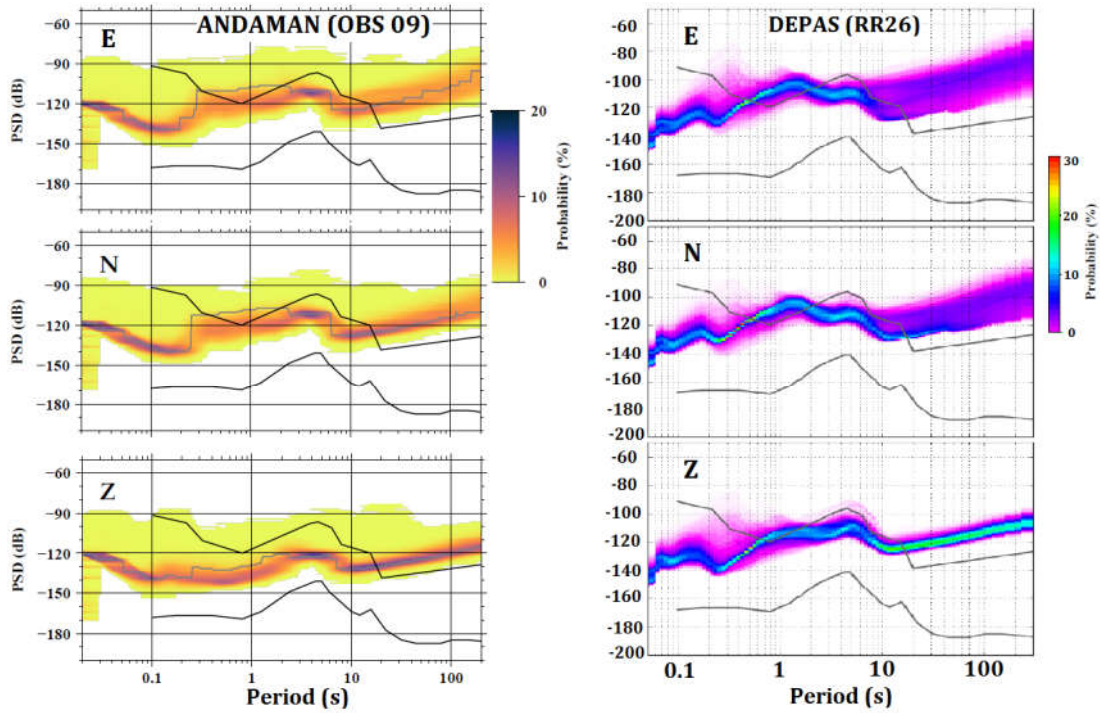


Figure 5. Comparison of Andaman network with RHUM-RUM Network. Right part of the figure is reproduced from the noise spectral plots of Rhum-Rum network and left part of the figure is from Andaman network (OBS09).

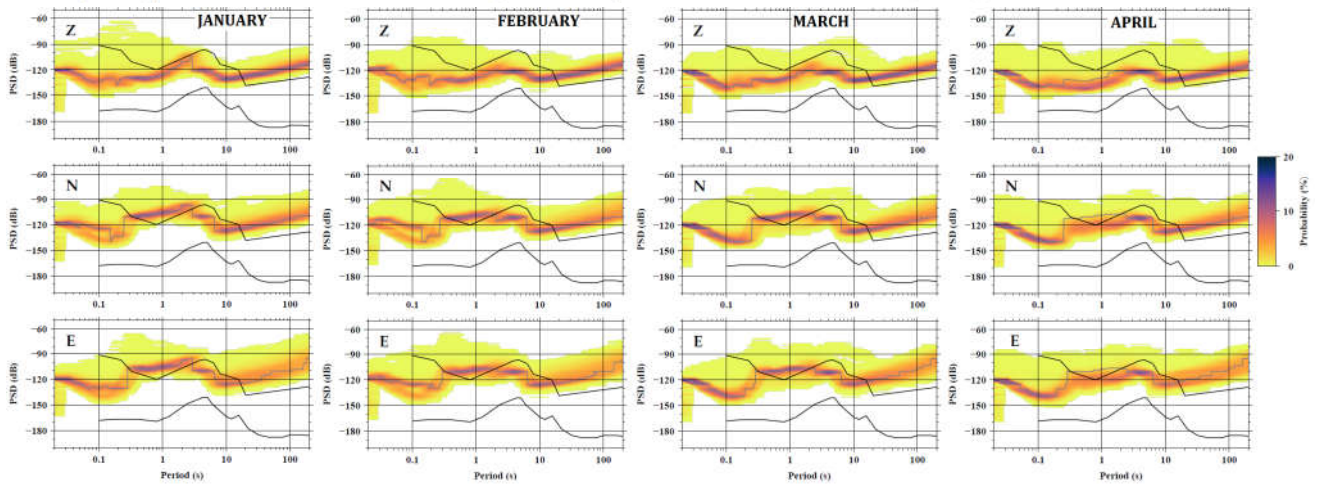


Figure 6. Monthly trends of the seismic noise at the station OBS09 in Andaman for the three components (Z, N, E), indicated in the upper left corner of each plot.

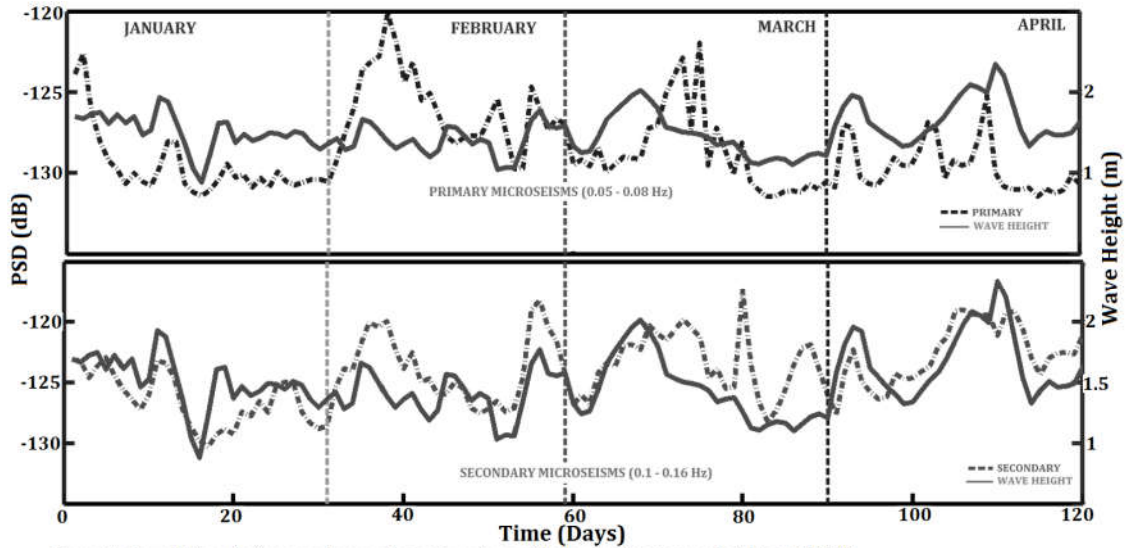


Figure 7. Correlation of primary and secondary microseisms with the significant wave heights at OBS 03

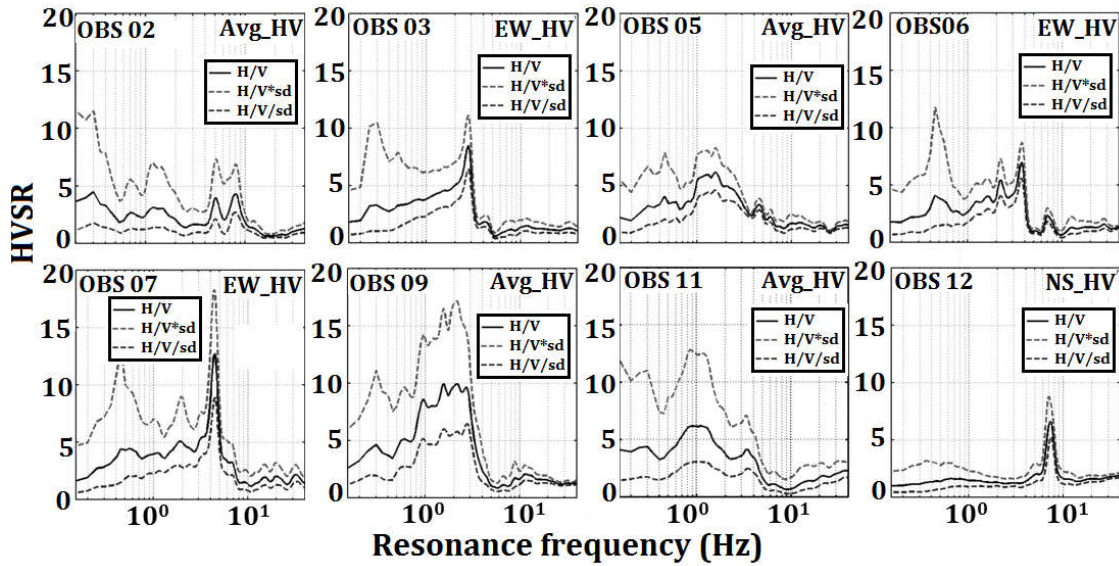


Figure 8. Site response parameters (fundamental frequency and amplification factor) of OBS stations using HVSr. Solid line is the mean curve ( $H/V$ ) and dashed lines are  $H/V*sd$  and  $H/V/sd$  ( $sd$ : standard deviation).

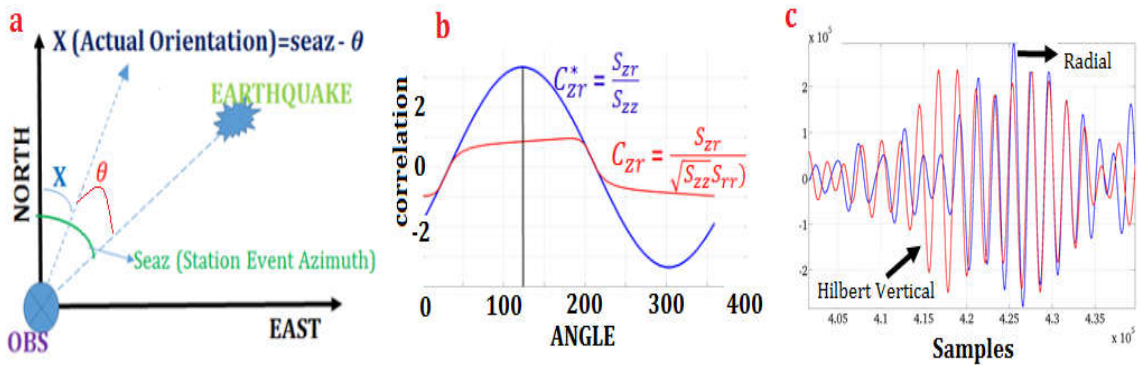


Figure 9. Working methodology of estimation of horizontal orientations of OBS stations. (a) Coordinate system and terms used to determine the accurate horizontal orientation of OBS stations. (b) Correlation coefficient between  $C_{zr}$  and  $C_{zz}$  as a function of possible orientation angle. Correlation coefficient is used to determine the orientation angle; Normalized correlation coefficient  $C_{zr}$  is for quality control; vertical line represents maximum  $C_{zr}$  at which the orientation is measured. (c) Correlation between radial and Hilbert transformed vertical for a given orientation obtained in (b)

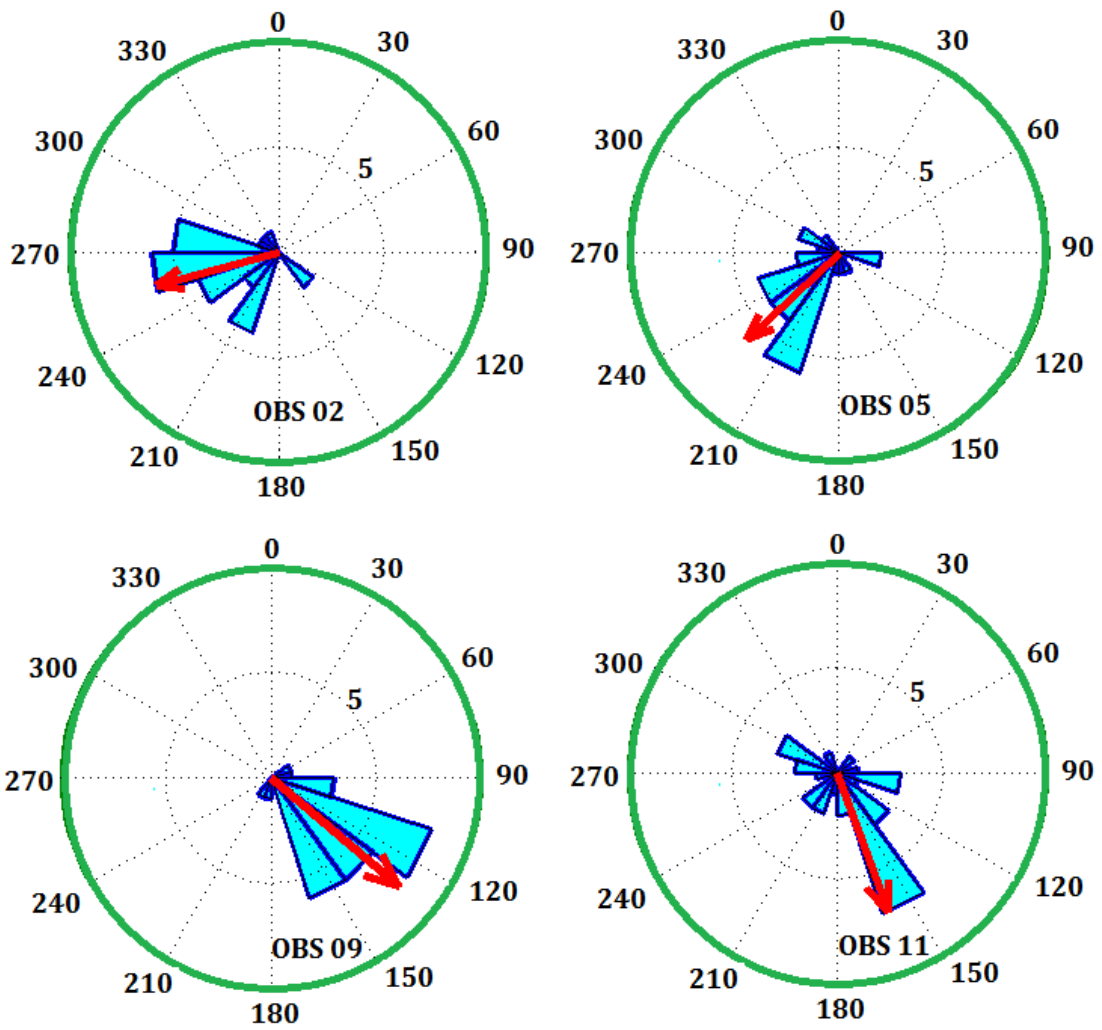


Figure 10. Polar orientation of four OBS stations measured from 30 teleseismic events; Arrow represents the mean orientation.



Table 1:

S.No	Station	Latitude (deg)	Longitude (deg)	Depth	Geological setting
1	OBS 01	7.903	91.698	3900	Indian plate close to subduction
2	OBS 02	7.741	94.129	1832	Off nicobar Islands
3	OBS 03	8.871	93.715	4183	Fore arc basin
4	OBS 05	9.901	95.073	1969	Sewell Sea mount
5	OBS 06	10.58	94.334	3439	Back arc Spreading center
6	OBS 07	10.908	94.731	3611	Back arc Spreading center
7	OBS 09	11.827	94.024	2264	Alcock Sea mount
8	OBS 11	9.541	93.168	1650	Fore arc basin
9	OBS 12	10.666	91.379	3485	Accretionary prism

Table 2:

Station	Horizontal component	$f_0$ (Hz)	$A_0$ (Criteria iii)	$\sigma_f$ (Criteria v)	$\varepsilon(f_0)$	$\sigma_A$ (Criteria vi)	$\theta(f_0)$	$A_{H/V}(f)$ (Criteria i)	$A_{H/V}(f^*)$ (criteria ii)	$f_0 \pm 5\%$ (Criteria iv)	Reliable H/V	Criteria Failed	Clear H/V
OBS 02	Avg	5	3.88	0.47	0.25	1.86	1.58	*	*	✓	✓	i,ii,v,vi	No
	Avg	8	4.26	0.5	0.4	1.6	1.58	*	✓	✓	✓	i,v,vi	No
	NS	8	5.63	0.49	0.4	1.77	1.58	✓	✓	✓	✓	v,vi	No
	EW	5	4.1	0.47	0.25	3.78	1.58	*	*	✓	✓	i,ii,v,vi	No
OBS 03	EW	2.8	8.44	0.05	0.14	1.31	1.58	✓	✓	✓	✓	--	Yes
OBS 05	Avg	1.5	6.14	0.32	0.15	1.34	1.78	*	*	✓	✓	i,ii,v	No
		4.5	3.31	0.15	0.22	1.16	1.58	*	✓	✓	✓	i	Yes
	NS	1.6	5.00	0.27	0.16	1.42	1.78	✓	*	✓	✓	ii, v	No
		4.6	4.1	0.15	0.23	1.21	1.58	*	✓	✓	✓	i	Yes
	EW	1.5	6.9	0.31	0.15	1.38	1.78	✓	✓	✓	✓	v	Yes
6		2.91	0.16	0.3	1.27	1.58	*	✓	✓	✓	i	Yes	
OBS 06	EW	2.2	5.39	0.07	0.11	1.36	1.58	*	*	✓	✓	i,ii	No
		3.7	6.95	0.08	0.18	1.24	1.58	*	✓	✓	✓	i	Yes
		7	2.31	0.26	0.35	1.28	1.58	*	✓	✓	✓	i	yes
OBS 07	EW	1.9	5.05	0.10	0.19	1.7	1.78	*	*	✓	✓	i,ii	No
		4.5	12.7	0.05	0.22	1.43	1.58	✓	✓	✓	✓	none	Yes
OBS 09	Avg	2.1	10	0.47	0.11	1.65	1.58	✓	✓	✓	✓	v,vi	No
	NS	1.5	9.2	0.42	0.15	1.79	1.78	✓	✓	✓	✓	v,vi	No
	EW	2.1	10.7	0.67	0.11	1.76	1.58	✓	✓	✓	✓	v,vi	No
OBS 11	Avg	1	6.14	0.48	0.1	2	2	*	*	✓	✓	i,ii,v	No
		3.1	4.11	0.50	0.16	1.69	1.58	*	✓	✓	✓	i,v,vi	No
	NS	0.9	3.21	0.54	0.13	1.62	2	*	*	✓	✓	i,ii, v	No
		4	3.27	0.16	0.2	1.84	1.58	*	✓	✓	✓	i,v	No
	EW	0.9	7.1	0.48	0.13	2.46	2	*	*	✓	✓	i, ii, v,vi	No
		3.3	5.1	0.55	0.17	1.85	1.58	*	✓	✓	✓	i,v,vi	No
OBS 12	NS	7.2	6.56	0.22	0.36	1.3	1.58	✓	✓	✓	✓	none	Yes